ORIGINAL PAPER

NEURAL NETWORK CLASSIFICATION OF LITHOLOGICAL UNITS BASED ON INTEGRATED RADAR AND MULTISPECTRAL DATA

**Naer RAHMANI [1]), H. RANJBAR [1]) *,
H. NEZAMABADI-POUR [2]) and E. J. M. CARRANZA [3, 4])**

[1]) *Department of Mining Engineering, Shahid Bahonar University of Kerman, Kerman, Iran*
[2]) *Department of Electrical Engineering, Shahid Bahonar University of Kerman, Kerman, Iran*
[3]) *Department of Geology, University of the Free State, Bloemfontein, 9300, South Africa*
[4]) *Discipline of Geological Sciences, School of Agricultural, Earth and Environmental Sciences, University of KwaZulu–Natal, Westville Campus, Durban 3629, South Africa*

Corresponding author's e-mail: h.ranjbar@uk.ac.ir

ABSTRACT

Geological mapping of exposed geologic units of Earth surface is a common and important activity for geologists. This process is the first step of geological prospecting. Remote sensing can provide useful driven data for further studies and also it reduces the time and cost of this process. Sometimes it is possible that some lithologies have similar spectral responses while they have different surficial texture properties. Geological units of the Earth surface are more separable by including their textural properties along with their spectral behaviour in remote sensing so authors used spectral-Radar data integration with novel idea which is named Radar data resultant vector in this study. In this paper, two different neural network methods (Neural Pattern Recognition and Neural Net Fitting) were implemented in Matlab environment for lithological classification using two different input datasets, namely (1) only multispectral data and (2) integrated Radar-multispectral data. The reason was to evaluate the performance of Spectral-Radar fused data in lithological classification in comparison with the spectral data alone. The results show that integrated Radar-multispectral data results in better classification of lithological units due to the integration of surficial textural parameters and spectral responses of such surficial features. The results also showed that the Neural Pattern Recognition method (NPRTool) performed better than Neural Net Fitting (NFTool) method. The results further show that, among the three different algorithms of the Neural Net Fitting method (i.e., Levenberg-Marquardt, Bayesian Regularization, and Scaled Conjugate Gradient), the Levenberg-Marquardt performed best.

1. INTRODUCTION

Mineral exploration is a complicated, multi-task process; however, this can be achieved through a series of sub-projects whereby every sub-project contributes somehow to the desired outcome (i.e., deposit discovery). Geological mapping is a major sub-project of mineral exploration. It is a time- and cost-consuming process, which needs up-to-date approaches and methods to enhance the quality of the lithological mapping process aside from reducing the cost and time of project implementation. Satellite images (as toolkits) and remote sensing techniques (as approaches) provide geologists up-to-date capability for lithological mapping to assist mineral exploration in reduced time and cost.

Involving remote sensing and satellite images in geological investigations and the Earth exploration tasks entails significant fusion of multi-source data. This ensures improvement in spatial resolution to achieve better results with detailed information, though, this is not the only advantage we can expect from data fusion (Yuhendra et al., 2012). Fusion of spectral datasets with ancillary data, fusion of multi-sensor images from Short-wave infrared (SWIR) and visible and near-infrared (VNIR) ranges, and data fusion in different levels are examples that can benefit lithological mapping and mineral exploration.

Geological investigations using spectral images focus on different responses of index minerals because of their absorption and reflection properties depending on the spectral resolution of a sensor. Therefore, based on different mineralogical compositions, every lithologic unit has its own spectral response in satellite image bands. However, it is possible to have a re-formed lithology due to weathering and oxidation conditions that has transported from the source rock with similar responses as the in-situ lithology. In such problems, the key to distinguish the initial lithology from the weathered or transported lithology is to pay attention to their textural properties. Whereas, medium resolution multispectral images have no data about textural properties of the Earth's surface, RAdio Detection and Ranging (Radar) data contain useful textural properties because of their polarimetric data recording (Pour and Hashim, 2014). Therefore, fusion of Radar and multispectral data offers integration of

surficial texture of lithologies with their spectral responses for enhanced lithologic discrimination (Pal et al., 2007).

Fusion of Radar and multispectral data for remote sensing has been applied mostly for classification of land-use (e.g., Joshi et al., 2016; Yuan et al., 2020; Palaniyandi et al., 2021; del Valle et al., 2023) and land cover (e.g., Kulkarni et al., 2019; Zhang et al., 2021; Montanaro et al., 2022; Righini et al., 2022), and for monitoring of crops (e.g., Cloutis et al., 1999; Upreti and Kumar, 2021; Mouret, 2022; Cheng et al., 2023) and forest (e.g., García et al., 2018; Vafaei et al., 2021; David et al., 2022; Movchan et al., 2023).

The number of studies about applications of Radar-multispectral data fusion for geological mapping is limited and continually is increasing by time (Thurmond et al., 2006; Grebby et al., 2011; Zoheir et al., 2019; Rahmani et al., 2020; Kamal El-Din et al., 2021; Hajaj et al., 2022; Zafaty et al., 2023). Thurmond et al. (2006) used integrated Enhanced Thematic Mapper Plus (ETM+), Advanced Spaceborne Thermal Emission and Reflection Radiometer (ASTER), Spaceborne Imaging Radar (SIR), RADARSAT-1 and Digital Elevation Model (DEM) data for geologic mapping in arid regions. They used SIR-C/X-SAR L-Band (Synthetic Aperture Radar) data with HH (Horizontal-Horizontal) polarization for individual lava flows in Quaternary. RADARSAT C-band (with HH polarization) aside ETM+ VNIR data were used to visualize extensional imbrication fans and finally morphologically structures in rhyolite flows were mapped by RADARSAT C-band with HH polarization integrated with ASTER VNIR and SWIR data. Grebby et al. (2011) used airborne Light Detection and Ranging (LiDAR) data and Airborne Thematic Mapper images for Self-Organizing Map (SOM) classification for lithological mapping in a vegetated area of Troodos ophiolite in Cyprus. They showed that airborne SAR and multispectral data could help to map complex and vegetated lithologies with better results. Zoheir et al. (2019) used Advanced Land Observing Satellite (Alos) Phased Array L-band Synthetic Aperture Radar (PALSAR) and sentinel-1B data for visual and automatic line extraction and finally integrated these data with multispectral data (ASTER and Landsat8 OLI) for interpretation of geological structures. Rahmani et al. (2020) used the Radar and multispectral data fusion by using intensity-hue-saturation and principal component analysis for lithology and structural mapping.

In this study, we tried semi-unsupervised lithologic classification with shallow neural network algorithm applied to two different data types, namely: (I) only multispectral and (II) integrated multispectral and Radar data. The objectives of this study were (1) to evaluate the success of using neural networks and integrated Radar-multispectral data in lithological remote sensing, (2) to propose a suitable neural network method for lithological mapping by remote sensing and (3) to compare the performance of using integrated Radar-multispectral data with performance of using non-integrated data. The innovations of this study are (a) combining Radar data polarization components (HH and HV) with a simple mathematical method, (b) pattern recognition techniques for classification/mapping of lithologic units based on integration of polarized Radar and multispectral data, and (c) improving data content of combined Radar data polarizations which was generated by resultant vector. These concepts and techniques have been used before for remote sensing classification/mapping of lithologic units based on integrated Radar-multispectral data but the novel combination method for HH and HV polarizations in this study is the creative core of this paper.

- **Geological setting**

Test site of this study is located in Kerman Copper Belt (KCB), which is a well-known area as far as its copper potential concern; therefore, this area is a good choice for assessing the remote sensing results. The KCB is located in the Kerman province, in southestern part of Iran (Fig. 1). The KCB arc magmatism formed two different complexes, one is the Bahr-Aseman complex (with Middle Eocene age) and the other is the Razak Complex (Upper Eocene) (Dimitrijevic, 1973a; Hassanzadeh, 1993). Calk-alkaline (basaltic to rhyolitic) lava flows and pyroclastic materials were the main products of the KCB arc magmatism. Some plutonic bodies (with batholith size and Eocene-Oligocene age) were intruded into Eocene volcano-sedimentary successions. Some plutonic bodies were mainly granites to diorites and locally gabbro (characterized by high- to Medium-K calk-alkaline affinity) with granular texture (Dimitrijevic, 1973a; Ghorashi-Zadeh, 1978; McInnes et al., 2003; Atapour, 2007; Shafiei et al., 2009).

Jebal-Barez type granitoids were named after a local mountain where they occur extensively (Dimitrijevic, 1973a) and many studies reported that they have no major metallic mineralization. The KCB arc magmatism continued into Middle Oligocene (Dimitrijevic, 1973a; Hassanzadeh, 1993) and magmatic reactivation happened to form numerous shallow intrusives (continued to Late Miocene and Pliocene) in a post-collisional tectonic setting (Atapour, 2007; Shafiei et al., 2009) with compositions ranging from diorites and quartz-diorites to granitoids (known as the Kuh-Panj type granitoids) and passing through the older volcanic and plutonic bodies (Ghorashi-Zadeh, 1978; Hassanzadeh, 1993; McInnes et al., 2003). The Kuh-Panj type granitoids (High-K calk-alkaline), which present typical features of I-type magmas (Atapour, 2007), are associated with major porphyry type mineralization (Dimitrijevic, 1973a; Alirezaei and Hassanpour, 2011). The KCB arc magmatism also generated dacites during Neogene, and finally Dehaj type intrusions (varying from dacite to rhyolite and locally andesite) (Dimitrijevic, 1973a; Hassanzadeh, 1993). This last magmatic activity in the
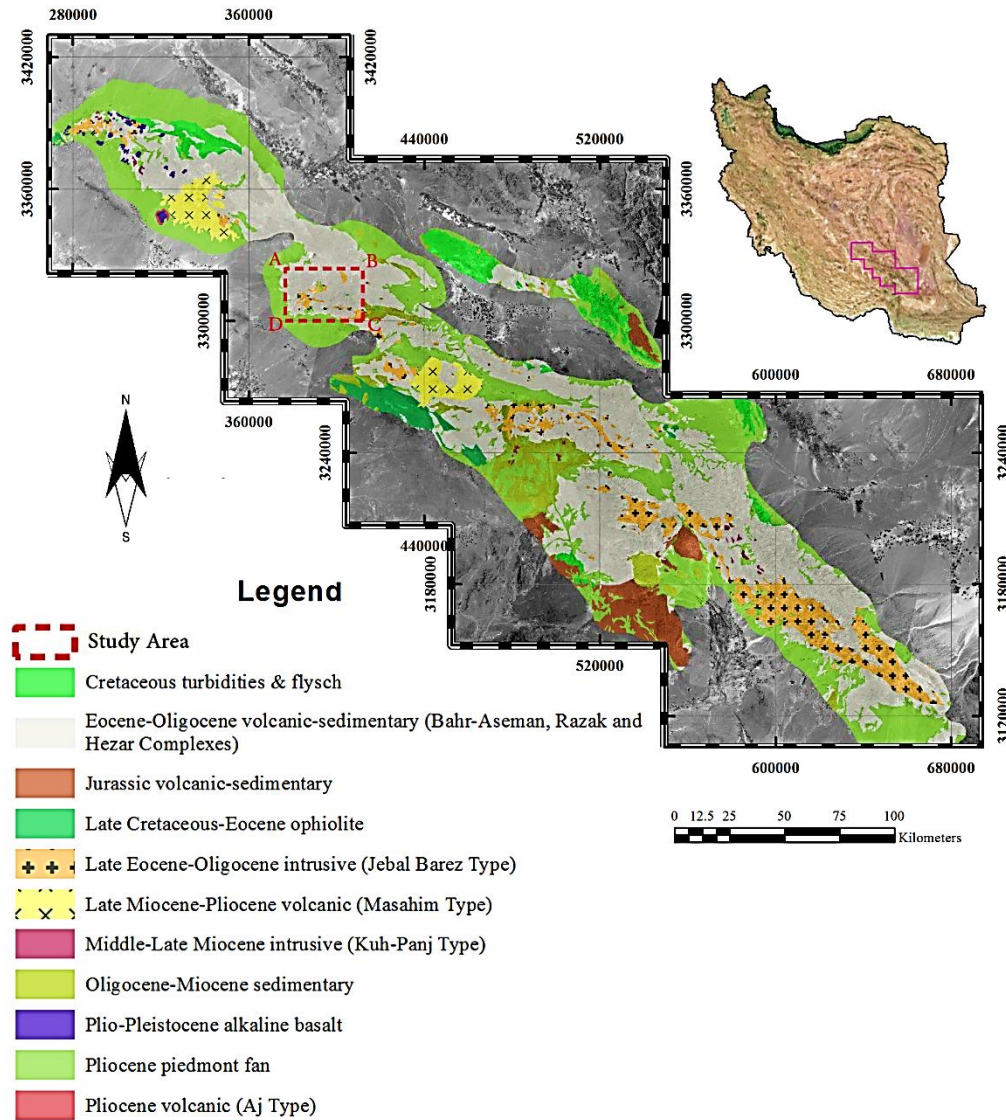
Fig. 1   Simplified geological map of the KCB area (Dimitrijevic, 1973a; Alimohammadi et al., 2015; Sabzehei et al., 1994).

KCB took place in Plio-Quaternary and is represented by olivine-alkali basalts, foidolites, and lamprophyres (Dimitrijevic, 1973a; Hassanzadeh, 1993; Atapour, 2007). Sedimentation process during Miocene produced large amounts of sandstone, conglomerate and arenites especially in the southern parts of the area. Calk tufa represents sedimentary features formed in the Quaternary; because of activities of hot springs associated with volcanic rocks.

In the study area, the oldest rocks are volcanic rocks of Eocene age. They are composed of mostly agglomerates, tuffs, andesite, trachyandesite, trachybasalt and basalt, which belong to the Razak Formation. These volcanic rocks were later intruded by intrusive bodies (diorite, quartz diorite, monzonite and granodiorite) of Oligocene age. These intrusive bodies caused the formation of several porphyry copper deposits in the area such as SarCheshmeh, Darreh Zar, Sereidun, Sarkuh, Hosein Abad, Bagh

Khoshk and Kuh Panj (Fig. 2). Quaternary dacites mark the final stage of volcanic activities in this area. During the Miocene, conglomerates with pebbles of volcanic and intrusive rocks were deposited in the southern and northern parts of the area. The Calc-tufa, alluvial sediments and gravel fans are the Quaternary features in the area.

2. DATA AND METHODOLOGY

In this study, three datasets from Advanced Spaceborne Thermal Emission and Reflection Radiometer (ASTER), Landsat7 Enhanced Thematic Mapper Plus (ETM+), and ALOS Phased Array type L-band Synthetic Aperture Radar sensors were used in ENVI, ArcGIS, and Matlab environments. Landsat7 ETM[+] was used instead of Landsat8 data because of more similarity to other above-mentioned data based on time of imaging. The satellite images were integrated by using layer stacking after applying
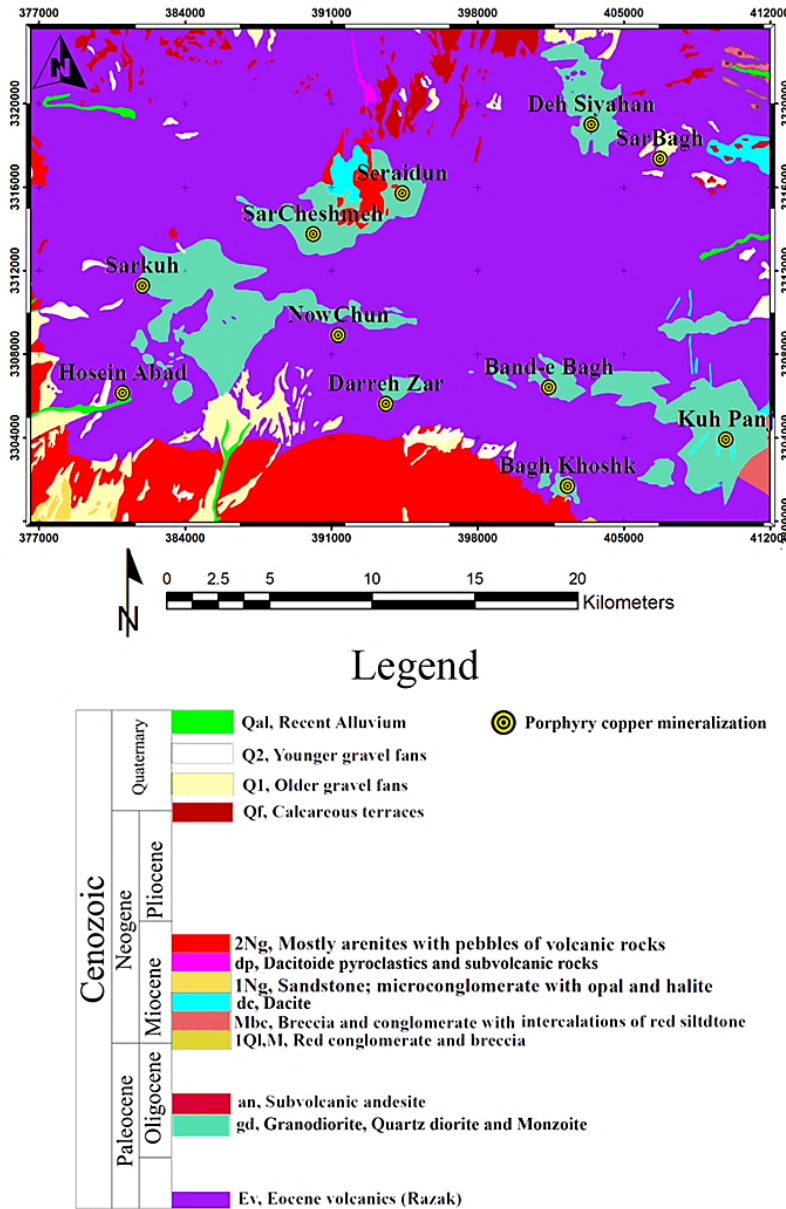
Fig. 2 Geologic map of study area based on Pariz (Dimitrijevic et al., 1971a), Chahargonbad (Dimitrijevic, 1971), Rafsanjan I (Dimitrijevic et al., 1973b) and Rafsanjan II (Dimitrijevic et al., 1971b) geologic maps.

necessary preprocessing methods (FLAASH correction for ASTER data, applying log function and 8-bit stretching on ALOS data). A computer was used for image processing and for running soft computing algorithms. Details of the computer processor were as follows: Intel(R) Core(TM) i7-2630QM CPU @ 2.00 GHz; system type: 64-bit operating system; total hard disc space: 1 TB; and installed memory (RAM): 8.0 GB

In 1972, the Landsat earth observation program was introduced and since then a new era of global land cover and land-use monitoring started. The Landsat program is the longest-running mission and it has launched eight different satellites into space. The Landsat 7 was launched on April 15, 1999, to continue

Earth observation with significant progress in precise numerical radiometry, spectral differentiation, and seasonally repetitive monitoring (Goward et al., 2001). The Landsat-7 ETM+ Level-1 products consist of L-1TP, L-1GT, and L-1GS products (Miao et al., 2019). In this paper, a L-1TP product (LE07_L1TP_160039_20000807_20170210_01_T1) covering area scene was used in this study (Table 1). L-1TP products are calibrated radiometrically and are orthorectified using ground control points (GCPs) and digital elevation model (DEM) data to correct the relief displacement (USGS, 2019).

The Terra satellite was launched into space in December 1999 as part of NASA's Earth Observing System program. It carried several remote sensing

Table 1 Landsat7 ETM+ scene details.

Sun Elevation	Sun Azimuth	Cloud Cover (%)	Acquisition Date	Acquisition Time (GMT)
62.59347914°	114.85462397°	0	2000/08/07	06:35:50

Table 2 ASTER scene details.

Sun Elevation	Sun Azimuth	Cloud Cover (%)	Acquisition Date	Acquisition Time (GMT)
51.034772°	145.680211°	0	2004/03/11	07:02:56.338

sensors, one of which is the Advanced Spaceborne Thermal Emission and Reflection Radiometer (ASTER) instrument. The ASTER sensor is a multi-spatial, spectral, and radiometric resolution imager (Abrams and Hook, 2002; Abrams and Yamaguchi, 2019; Yuan et al., 2020; Çolak and Sunar, 2023). It is the most widely used sensor for geological purposes and it offers great abilities for geologists to detect and enhance hydrothermal alteration mineral zones and lithological units (e.g., Pour et al., 2013; Pournamdari et al., 2014a, 2014b; Gabr et al., 2015; Amer et al., 2016; Guha and Vinod Kumar, 2016; Salem et al., 2016; Safari et al., 2018; Rani et al., 2019; Zhang et al., 2023; Nasab and Agah, 2023).

An ASTER level L1T scene covering the study area was obtained from the U.S. Geological Survey Earth Resources Observation and Science Centre (EROS). Details of this ASTER scene (AST_L1T_00303112004070256_20150503143507_69958) are presented in Table 2.

The FLAASH (Fast Line-of-sight Atmospheric Analysis of Spectral Hypercube) atmospheric correction (Anderson et al., 2002; Cooley et al., 2002; Li et al., 2023) was applied to the ASTER scene (both VNIR and SWIR bands). The FLAASH algorithm was implemented using the Mid-Latitude Summer (MLS) atmospheric and the rural aerosol models (Research Systems, 2003). ASTER VNIR and SWIR bands were resampled to 30-m spatial resolution using the nearest neighbour resampling method to preserve the original pixel values in the resampled images.

The ALOS satellite was launched into space on 24 January 2006 by the Japan Aerospace Exploration Agency (JAXA). It has a traveling altitude of 691 km above the Earth's surface. This satellite images the Earth's surface in 46 days repeating cycle. Three different remote sensing instruments are carried by ALOS satellite: The Panchromatic Remote-sensing Instrument for Stereo Mapping (PRISM), the Advanced Visible and Near-Infrared Radiometer type 2 (AVNIR-2), and the PALSAR (Almeida-Filho et al., 2009; Papale et al., 2023).

The PALSAR is an L-band SAR (synthetic aperture Radar) with multi-polarization ability that records great responses from vegetated areas, and, thus, it is a good tool for discriminating between fully vegetated, sparse vegetated, and open land areas. All three instruments on board ALOS benefit from a systematic observation strategy as a foreground mission, which helps to have stable wall-to-wall recordings with fine spatial resolution in all instruments (Rosenqvist et al., 2014). Radiometrically Terrain Corrected (RTC) products are geometrically and radiometrically terrain corrected products and they are distributed at two resolutions (RT1 & RT2) (Logan et al., 2014; Li et al., 2020). RT1 products have a 12.5 m pixel size spatial resolution whereas RT2 products are generated with 30 m pixel size (Rosenqvist et al., 2007). All ALOS PALSAR scenes that were used in this study (to fully cover the study frame) were RT1 products, and Table 3 shows detailed information about them.

2.1. RADAR DATA PREPARATION AND PROCESSING

RT1 data do not need further pre-processing steps. However, in this study, some changes were applied to ALOS PALSAR scenes as explained below.

Radar data must be rescaled to 8-bit spectral data to have the same power in the fusion process. Initial RT1 products have great variance in DN values. To remove the unwanted variance, it is recommended to apply a logarithmic operation on DN values and then to stretch data into 8-bit integers (using Gaussian stretch) (Bashir and Gilani, 2011).

Each polarization image contains useful data of the Earth's surface, and combining the data obtained from HH and HV polarizations helps to get a comprehensive idea of the study area. If we assume that every polarization image has a vectorized nature, it is possible to combine two perpendicular polarized images into one image by defining a resultant vector as is shown in Figure 3. In this research, the introduced resultant vector was used in all fusion steps and methods because of its information content as shown in Figure 4.

The HH&HV resultant vector image has the combination effect of both polarizations that is useful for differentiating different rocks based on the Radar return. This is discussed in the Discussion section. Figure 5 shows the Landsat 7 false color composite (6- A) which is stretched by decorrelation method in comparison with the Radar HH&HV Resultant image (5-B).

2.2. ARTIFICIAL NEURAL NETWORKS

Artificial neural networks (ANNs) are a small-scale scientific imitation of the human brain and nervous system; in other words, ANNs mimics the biological aspect of human neural network (Mehta et

Table 3   Metadata of ALOS PALSAR scenes.

Name	Path / Frame	Polarization	Acquisition Date	Off-Nadir Angle	Absolute Orbit
ALPSRP183900580	565/580	HH+HV	07/07/09, 18:50:36	34.3°	18390
ALPSRP087480580	564/ 580	HH+HV	09/15/07, 18:46:55	34.3°	8748
ALPSRP123510590	565/590	HH+HV	05/19/08, 18:46:17	34.3°	12351
ALPSRP087480590	564/590	HH+HV	09/15/07, 18:47:03	34.3°	8748

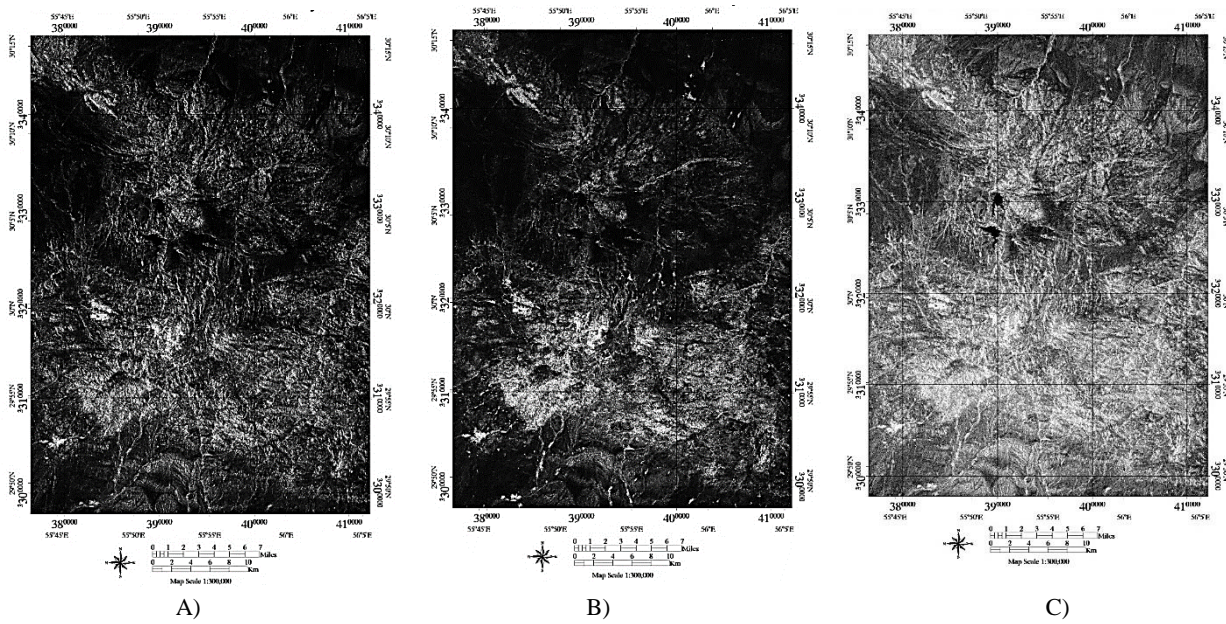A)   B)   C)

Fig. 4   HH (A) and HV (B) polarized images in comparison with HH&HV Resultant Vector (C).

$$\overrightarrow{Resultant\ Vector} = \sqrt{\overrightarrow{HH^2} + \overrightarrow{HV^2}}$$
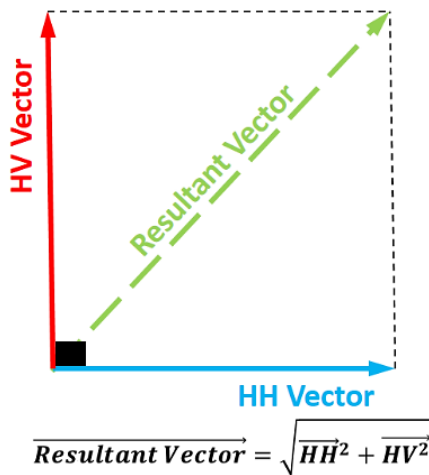
Fig. 3   Resultant vector for HH and HV polarizations.

al., 2016; Prisciandaro et al., 2023). It is called a network because of its interconnections between nodes (neurons) like a web. The human brain is a complex organ composed of billions of specialized cells called neurons. Each neuron acts as an information processing unit, transmitting signals to and from the brain. These neurons work together in intricate networks to enable the brain's remarkable capabilities. In contrast, artificial neural networks (ANNs) are computational models inspired by the structure and function of the human brain. While not as advanced as the biological brain, ANNs consist of interconnected artificial neurons or processing units. Typical ANNs have hundreds or thousands of these artificial neurons, far fewer than the billions found in the human brain. Despite the differences in scale and complexity, both biological and artificial neural networks share the common purpose of processing information. The human brain's neurons receive, process, and transmit electrochemical signals, while artificial neurons perform mathematical operations on input data. Both types of networks rely on the connections between their processing units to learn and adapt.

The architecture of ANNs is divided into two types, single and multi-layer. ANN benefits from a problem-solving approach instead of following a set of instruction without any intelligence (Kose and Arslan, 2017). The main stage in ANN is learning or
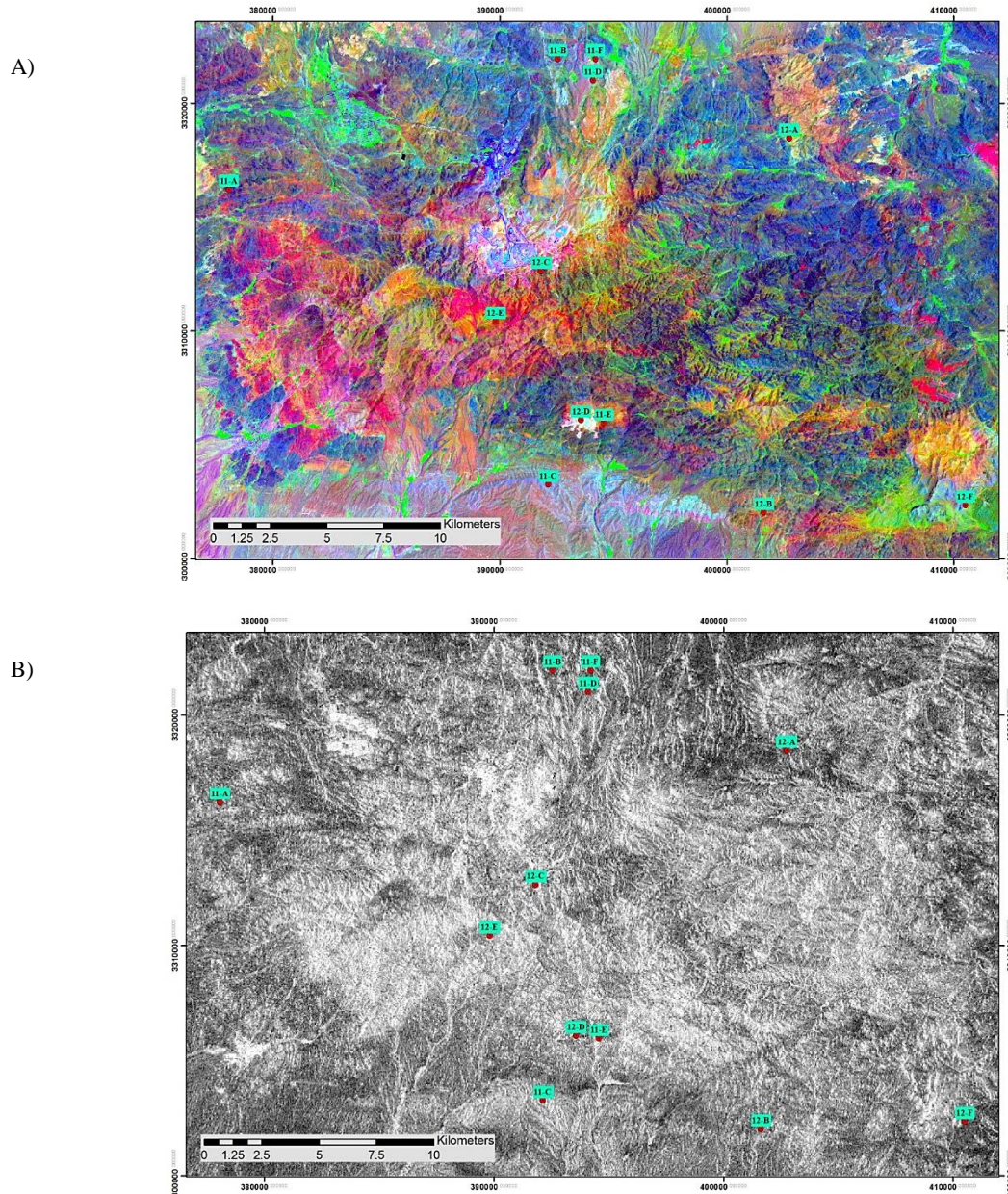
Fig. 5   A-False Color Composite of bands 7-4-1 in red, green and blue with decorrelation stretch. B- HH&HV Resultant Vector. The numbers on these images are the index of photographs for Figures 11 and 12.

training, and so the quality of output is directly dependent on network structure, number of inputs and train epochs. Despite all of the advantages of ANNs, the over-fitting problem and longtime duration of training are two weak aspects of ANNs (Tetko et al., 1995). In simple (or shallow) neural networks, there is one single hidden layer. However, in deep learning neural networks, there are more than one hidden layer (Delalleau and Bengio, 2011) (Fig. 6).

For better explanation of this study work, it is important to introduce some phrases and idioms.

- Feedforward network: in this type of ANN, connections between nodes do not make a cycle. This means that an output of a node will not be an input of past node and it only goes forward (Bebis and Georgiopoulos, 1994). Feedforward networks are the simplest and mostly used networks.

- Sigmoid neuron: perceptrons have binary outputs and, in non-linear classification problems, are not usable. In such problems, sigmoid neurons with output that vary between 0 and 1 are used. Sigmoid function has smoother results in comparison with step function (A function that increases or decreases rapidly from one constant value to another) (Neapolitan and Neapolitan, 2018).

- Softmax output layer: output of a softmax layer is a set of positive numbers, which sum up to 1. In other words, output of a softmax layer is a probability distribution (Neapolitan and Neapolitan, 2018).
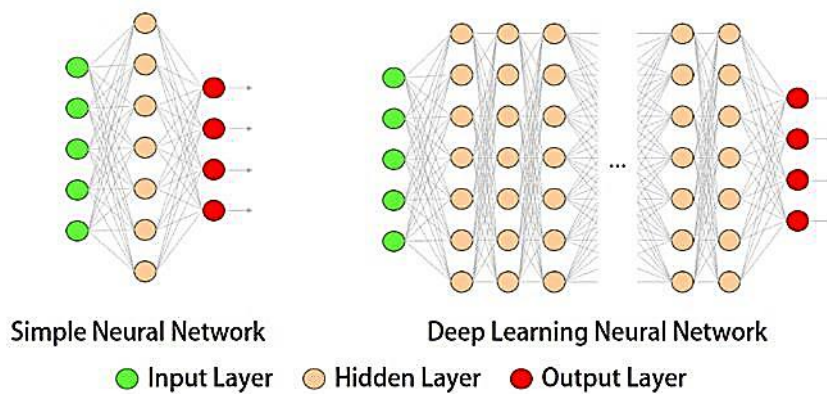
Fig. 6   Shallow vs. deep neural networks.

Some studies used ANNs to integrate different data types of remote sensing sources to gain better results (e. g., Bruzzone et al., 1999; Berberoglu et al., 2000; Joshi et al., 2016)

2.3. DATASET PREPARATION

All the bands were converted to an M by N matrix based on DN values in next step every band matrix was converted to a vector format (with one by M*N values). All band vectors merged together to form a new matrix which every column is related to a unique band and every row is DNs of the pixel in all bands. This matrix includes all the data about study area. This matrix was used in Matlab environment.

2.3.1. TRAINING DATASET

For every unique lithology, some areas were enclosed based on a-priori information from field studies and reconnaissance. About 10 % of pixels covering the scene were selected as labelled pixels. Number of train pixels is a result-based problem and is related to neural network architecture, complexity of dataset, type and amount of inherent noise in dataset, etc. Some studies determine the number of train pixels based on degree of freedom (DoF) in neural network and apply the 10 times rule on DoF (Kohli et al., 2017). Some studies propose to use at least 50 train pixels for every class randomly (Bharatkar and Patel, 2013). Pixels were addressed by row and column and their corresponding values of every band assigned to them. A vector dataset from training data was prepared and it was used as a target input for neural net tools in Matlab. Detailed information about training pixels is presented in Table 4.

All pixels in Table 4 were divided into three random categories in every train epoch, 70 % for train set, 15 % for validate set, and 15% for test set. Datasets are usually partitioned into training, validation and testing subsets. Unfortunately, there is no clear rule about what proportions of the data to use. However, it is important that training data must have greater proportion compared to testing and validation data. Many studies used proportions of 70-15-15, some used 80-10-10 and others used 60-20-20. Here, we chose 70-15-15 proportions for splitting the data into training, validate validation and testing subsets (e. g., Awoyera et al., 2020; Liu et al., 2020; Edoho et al., 2018).

2.3.2. NEURAL NET PATTERN RECOGNITION

In neural net pattern recognition, inputs are classified into a set of target categories. The NPRTool in Matlab environment is an app applied commonly to vectorized input data with a related target vector. The NPRTool benefits from a two-layer feed-forward network, with sigmoid hidden and softmax output neurons (Bansal and Chhikara, 2014). The NPRTool uses scaled conjugate gradient back-propagation to train input data (Azhar Omar et al., 2013). Samples are divided into three parts (training, testing, and validation). Samples for training are presented to a network for learning. After training (which depends on no changes in generalization), validation samples are used to evaluate system generalization. Testing samples have no effect on the training process and they are used to measure network performance during and after training (Bansal and Chhikara, 2014). Networks constructed by the NPRTool in this study have two layers, 10 neurons in hidden layer, and 18 neurons in output layer. The number of input neurons based on input data varies between 15 and 18 (Figs. 7 and 8).

2.3.3. NEURAL NET FITTING

This method was applied using the NFTool app, implemented in Matlab environment. The NFTool creates a 2-layer feed-forward network with sigmoid hidden neurons and linear output neurons (Ibáñez Civera et al., 2011). All tested networks have 10 neurons in hidden layer. Three different training algorithms were used to evaluate the results (i.e., Levenberg-Marquardt, Bayesian Regularization, and Scaled Conjugate Gradient).

The Levenberg-Marquardt algorithm typically needs more memory to solve problems, but solving time is reduced. In this algorithm, training stops when no significant improvement occurs in generalization (defined by the mean square error of the validation

Table 4 Number of learning pixels for every class.

| Class	Number of train pixels	Percentage in all pixels of dataset
Mostly arenites with pebbles of volcanic rocks (2Ng)	24857	2.67 %
Alluvial	1886	0.20 %
Altered Granodiorites (Altered Gd)	2898	0.31 %
Dacites (dc)	1767	0.19 %
Dacitoide pyroclastics (dp)	487	0.05 %
Alternation of dacitic tuff breccia and hyaloporphyritic dacite (Edv)	3301	0.36 %
Andesitic volcanic breccia, with lava flows (Eta)	4572	0.49 %
Granodiote (Gd)	15016	1.61 %
Breccia and conglomerate with interclations of red siltstone (Mbc)	2074	0.22 %
Dacitic tuff-breccia and lithic tuff, green (Mda)	1841	0.20 %
Razak Volcanics	983	0.11 %
Red Tuff	2412	0.26 %
Travertine	4385	0.47 %
Vegetation	311	0.03 %
Water	85	0.01 %
Eocene Volcanics	4472	0.48 %
Clac-Terraces	3361	0.36 %
Sum	74708	8.03 %
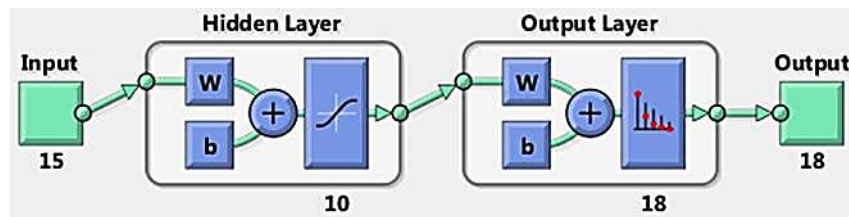
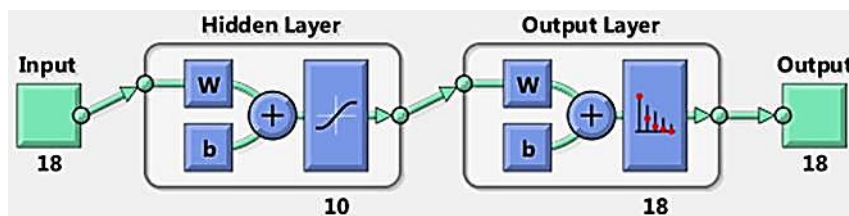**Fig. 7** Neural Net structure for the multispectral data input.

Fig. 8 Neural Net structure for integrated data input.

data). The Bayesian Regularization algorithm is the best choice for difficult, small, or noisy datasets. It needs more time to solve problems and training stops by minimizing the adoptive weight (regularization). The Scaled Conjugate Gradient algorithm occupies less memory for training time and it is controlled by improvement in generalization (Kumar et al., 2016).

2.4. ACCURACY ASSESSMENT

It is imperative to evaluate the classification results and to determine the accuracy of the classification method by comparing the results with ground truth information. A confusion matrix is a good calculation method for this purpose (Research Systems, 2003). In the calculation of the confusion matrix, we compared classification results with ground truth data, and finally, the result is comparable by numerical scales (such as overall accuracy, producer and user accuracies, Kappa coefficient, and errors of commission and omission).

The Kappa coefficient (k) is a measure of classification accuracy. It can be calculated as:

$$K = \frac{Po - Pc}{1 - Pc} \tag{1}$$

where Po (observed proportion of agreement between the two raters) denotes "observed agreement" and Pc "chance agreement" (expected proportion of agreement due to chance) (Research Systems, 2003). The Kappa coefficient varies between 0 and 1. If
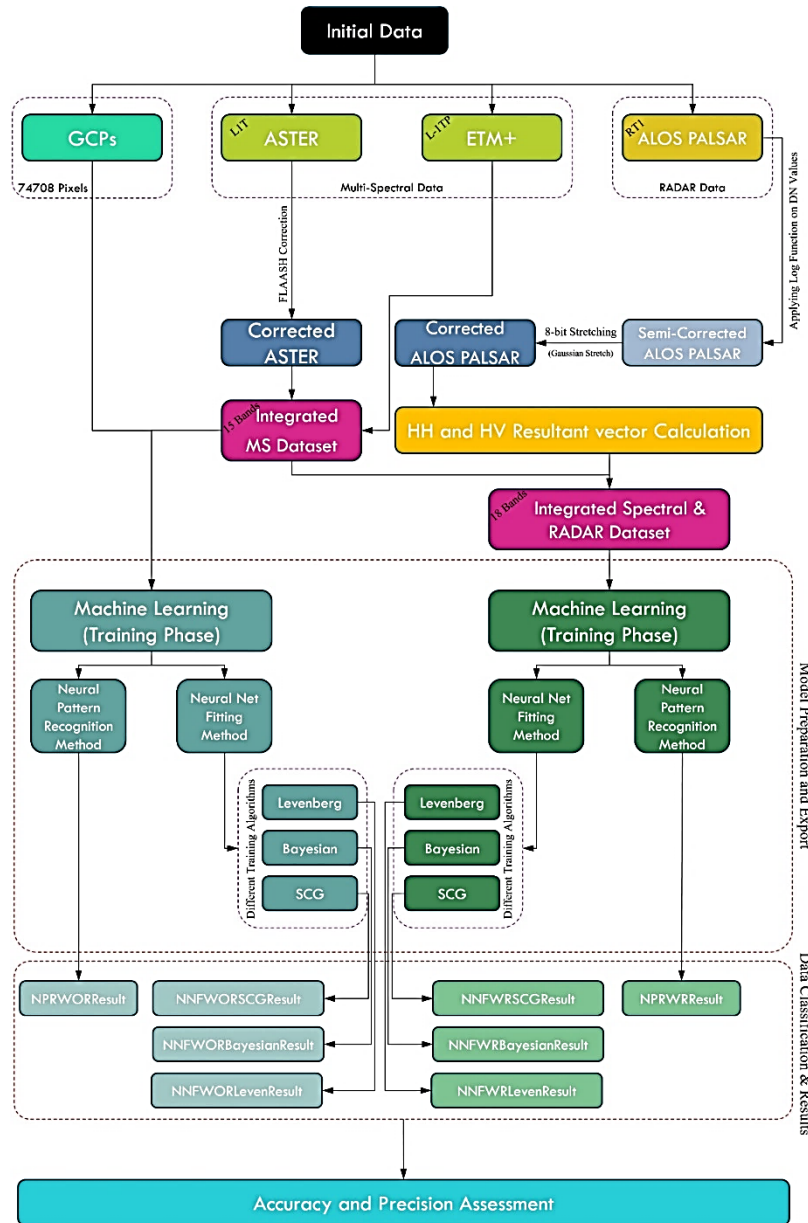
Fig. 9   Schematic view of the research methodology in this research (WR=With Radar, WOR=Without Radar).

Kappa coefficient equals 0, it means that there is no agreement between the classified result and reference data (bad classification) and if it is equal to 1, it shows that classification is the same as the reference data (best classification).

An error of commission represents pixels that belong to a class but classified into another class of interest. An error of omission represents pixels of ground truth data that were not classified into the correct class. The producer accuracy is a measure of omission error and it represents under-estimation, whereas user accuracy is a measure of commission error and it represents over-estimation (Research Systems, 2003). Schematic view of this research steps is presented in Figure 9.

3.   RESULTS

In this study, four different methods (implemented in Matlab environment) were used to evaluate the results of each method using integrated multispectral-Radar data and multispectral data alone. The NPRTool and NFTool applications in Matlab were used to apply the methods to these input datasets. All neural nets were structured with 10 hidden neurons. Table 5 presents the basic information about each method. Figure 10 shows the results of the methods mentioned in Table 5.

About 3 % of the pixels covering the scene (about 30000 pixels) were used as ground control points to evaluate the results of each method by using the confusion matrix. We checked the ground control points in the field, collected samples, and studied the lithologies under the optical microscope. Tables 6 and 7 present the related results.
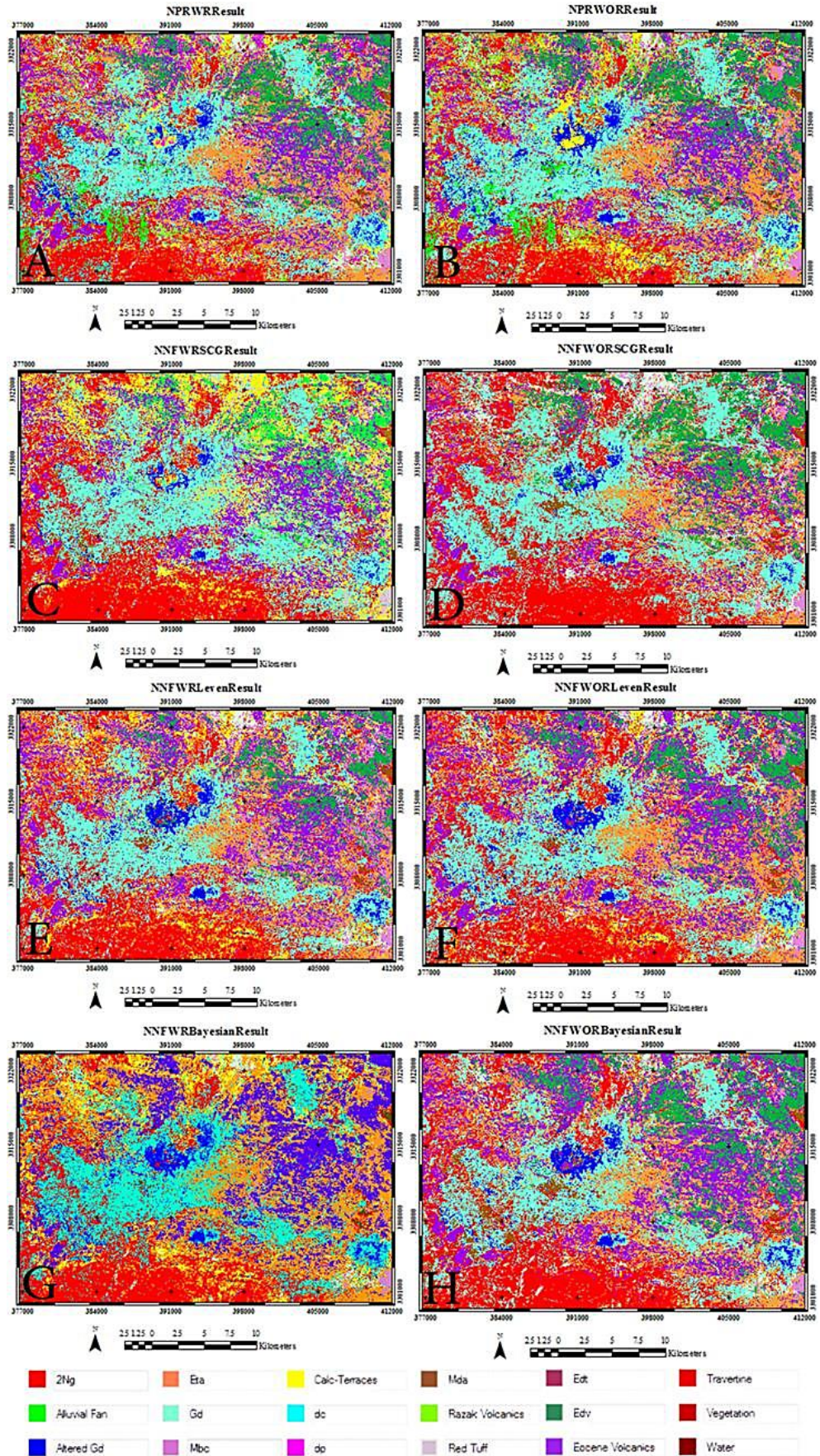
Fig. 10 Results of image classification based on different methods. The methods are listed in Table 5. The location of Figures 12-G and H is shown by dashed circle (10-A).

Table 5 Basic information about the applied methods.

	Input Data	Method	Train epochs	Train Error	Train Run Time	Output name
1	18 Inputs (ETM, ASTER, ALOS)	Neural Pattern Recognition	3	6.18 %	< 1′:00″	NPRWRResult (Figure 10-A)
2	15 Inputs (ETM, ASTER)	Neural Pattern Recognition	6	7.5 %	< 1′:00″	NPRWORResult (Figure 10-B)
3	18 Inputs (ETM, ASTER, ALOS)	Neural Net Fitting (SCG)	1	R=0.77	< 1′:00″	NNFWRSCGResult (Figure 10-C)
4	15 Inputs (ETM, ASTER)	Neural Net Fitting (SCG)	1	R=0.76	< 1′:00″	NNFWORSCGResult (Figure 10-D)
5	18 Inputs (ETM, ASTER, ALOS)	Neural Net Fitting (Levenberg)	1	R=0.84	< 1′:00″	NNFWRLevenResult (Figure 10-E)
6	15 Inputs (ETM, ASTER)	Neural Net Fitting (Levenberg)	2	R=0.83	2′:18″	NNFWORLevenResult (Figure 10-F)
7	18 Inputs (ETM, ASTER, ALOS)	Neural Net Fitting (Bayesian)	1	R=0.81	6′:41″	NNFWRBayesianResult (Figure 10-G)
8	15 Inputs (ETM, ASTER)	Neural Net Fitting (Bayesian)	1	R=0.82	8′:35″	NNFWORBayesianResult (Figure 10-H)

Table 6 The main information about the classification result of each method (red texts represent dataset of only multispectral and blue ones represent integrated Radar and multispectral dataset).

	NPRWOR	NPRWR	NNFWRLeven	NNFWORLeven	NNFWRBayesian	NNFWORBayesian	NNFWRSCG	NNFWORSCG
Overall Accuracy	80.09 %	79.36 %	72.89 %	70.54 %	73.45 %	67.97 %	61.88 %	60.34 %
Kappa Coefficient	0.7773	0.7697	0.6948	0.6677	0.6983	0.6393	0.5682	0.5509
Train Epochs	6	3	1	2	1	1	1	1
Train Error	7.50 %	6.18 %	R = 0.84	R = 0.83	R = 0.81	R = 0.82	R = 0.77	R = 0.76
Train Run Time	< 1′:00″	< 1′:00″	< 1′:00″	02′:18″	06′:41″	08′:35″	< 1′:00″	< 1′:00″

As it is shown in Figure 9, the top row in Table 6 represents the classification methods. A simple naming code was used to make it easier to understand. First three characters in every phrase indicate the classification method (NNF= Neural Net Fitting or NPR=Neural Pattern Recognition), the next phrase (WR or WOR) shows that the used dataset is integrated with Radar data or not (WR=With Radar and WOR=Without Radar). The probable next phrase is related to the type of used algorithm in NNF method

(i.e., Levenberg-Marquardt, Bayesian Regularization, and Scaled Conjugate Gradient).

Maximum overall accuracy is for NPR classification method (79.36 % and 80.09 %). In comparison between the two conditions of Radar-Spectral and only Spectral dataset for classification by NPR method, it was found that doubling the train epochs for pure spectral dataset, only result in improving the overall accuracy less than 1 % and in equal condition (similar train epochs) the

Table 7 Commission and omission values for each class by different methods (red texts represent dataset of only multispectral and blue ones represent integrated Radar and multispectral dataset).

		NPRWOR	NPRWR	NNFWRBayesian	NNFWRLeven	NNFWORLeven	NNFWORBayesian	NNFWRSCG	NNFWORSCG
Commission (%)	2Ng	2.63	4.3	**10.7**	13.64	16.89	21.21	22.24	26.35
	Alluvial	17.6	9.11	0	0	0	0	0	0
	Altered Gd	2.68	0	0	0	0.69	0.59	0	0
	dc	4.44	24.21	0	0	0	0	0	0
	dp	30.77	32.2	0	0	0	0	0	0
	Edv	51.08	59.19	0	54.19	51.55	61.76	54.62	61.22
	Eta	5	7.45	31.79	9.91	7.1	9.33	5.51	18.57
	Gd	40.79	39.21	39.14	37.69	46.26	39.86	56.52	62.92
	Mbc	37.9	7.78	28.04	44.4	43.17	28.04	40.08	40.08
	Mda	6.87	0	0	2.17	2.88	50.55	12.95	23.93
	Razak Volcanics	54.46	27.27	0	0	0	0	0	0
	Red Tuff	19.85	23.65	42.94	27.43	46.13	52.06	0	44.23
	Travertine	3.14	11.83	44.02	50.25	45.31	47.57	52.28	30.12
	Vegetation	0	0	0	0	0	0	0	0
	Water	0	0	0	0	0	0	0	0
	Eocene Volcanics	2.77	5.32	26.57	4.54	10.86	10.41	5.49	2.27
	Clac-Terraces	16.28	14.25	36.43	37.8	19.13	52.31	64.66	0
Omission (%)	2Ng	8.4	4.24	2.12	1.62	5.16	6.36	0.49	1.48
	Alluvial	11.16	15.4	100	100	100	100	100	100
	Altered Gd	40.25	52.36	33.16	31.62	40.55	30.29	79.98	69.82
	dc	66.67	44.19	100	100	100	100	100	100
	dp	10	0	100	100	100	100	100	100
	Edv	5.01	4.74	100	2.51	4.18	3.06	8.36	0.84
	Eta	5.52	3.87	6.35	14.64	13.26	14.09	29.01	15.19
	Gd	3.62	3	0	0.31	7.24	8.89	2.48	14.79
	Mbc	0	0	0	0	0	0	0	0
	Mda	3.94	0	9.63	0	0	0	10.37	8.15
	Razak Volcanics	51.58	41.05	100	100	100	100	100	100
	Red Tuff	40.06	13.17	42.3	51.82	45.38	54.34	88.52	59.38
	Travertine	3.14	8.21	3.86	3.86	2.9	3.62	11.59	14.25
	Vegetation	57.25	43.48	100	100	100	100	100	51.45
	Water	0	0	100	100	100	100	100	100
	Eocene Volcanics	35.89	49.59	8.4	40.46	35.53	41.83	38.63	56.71
	Clac-Terraces	20.88	15.66	32.42	34.89	48.9	91.48	66.21	100

result is more desirable for integrated Radar-Spectral dataset.

SCG algorithm for NNF method represented a poor classification result among all compared methods (with overall accuracies of 60.34 % and 61.88 %). As you can see, overall accuracy for integrated Radar-Spectral dataset is bigger than the only Spectral dataset in completely similar conditions.

The Bayesian Regularization algorithm for NNF method takes a long time to become fully trained and find a way to classify the data (in comparison with all other NNF algorithms). Classification of integrated Radar-Spectral dataset by this algorithm has the highest value of overall accuracy in all NNF classification results and in the next place, integrated dataset by Levenberg-Marquardt algorithm has the highest value for overall accuracy.

By subtracting the User's Accuracy from 100 %, the Commission error is measured and in a similar way by subtracting the Producer's Accuracy from 100 %, the omission error is calculated. Omission error is absolutely lower than Commission error value for Gd and Mbc classes, which means that misclassification is completely caused by classifying pixels from other classes to these classes (2Ng, Edv, Mda and Travertine classes have similar condition in most cases). Mbc class Omission error value is exactly equal to zero for all classification methods. Unlike those classes, Altered Gd, dc, Vegetation and Water classes have higher Omission error than Commission error values. This means that some pixels of these classes are classified into other classes in a wrong way. Misclassification of Water pixels is mainly concerned with high Omission error values (equal to 100 %) and only in NPR method results (either Radar-Spectral or only Spectral data) this value is equal to zero (note that Commission error is zero for both NPR results). In a similar condition, Mda class represents zero error value of Omission and Commission only in NPR classification method on integrated Radar-Spectral dataset. In addition, Razak volcanics and dp classes in most cases have higher Omission error values than Commission error.

3.1. FIELD CHECKS

After classification of the rocks by remote sensing, several points in the field were selected for checking. The rocks were examined in the field as well as in the laboratory for lithology and hydrothermal alteration style. Laboratory work included thin section studies under the optical microscope. Figures 11 and 12 demonstrate the selected lithologies and geological features that are discussed in the discussion section. The locations of the photographs in Figures 11 and 12 are shown in Figure 5.

4. DISCUSSION

Distinguishing rock types (lithological mapping) using optical remote sensing can be difficult, particularly for rocks with complex mineral compositions and those affected by hydrothermal alteration. While spectral properties are crucial, textural characteristics also play a significant role. These textures are related to the surface roughness, drainage patterns, and morphological roughness. To achieve the most accurate results, combining optical and radar imagery is often necessary.

Radar images have a high return on vegetated areas because of the cardinal effect. This has applications in structural interpretation such as fault location, as the linear features are better enhanced in the Radar images (Fig. 5-B). As the satellite images are acquired in a dry season, vegetation cover, except in the valleys, is poor and so there are good outcrops in the field. In some areas with higher elevation that receive snowfall in winter, vegetation and soil cover mask the lithology; however, mapping the lithologies is possible by remote sensing (Figs. 11-B and F). In some areas, volcanic rocks are hydrothermally altered, especially, in the vicinity of intrusive bodies (Figs. 11- E, 12-D and 12-E). In such cases, hydrothermal alteration does not allow the recognition of the original lithology by remote sensing. Argillic, phyllic and propyltic are the main types of hydrothermal alteration. The altered areas within the volcanic and the intrusive rocks show a low Radar return (Figs. 11-E, 12-C and D). It can be attributed to the smoother surface due to the weathering processes. Most of the unaltered volcanic rocks show higher Radar return because of their rough surfaces (Fig. 11- E).

The intrusive bodies have good rock exposures in the area, except in some locations with higher elevations, which are covered by soil and vegetation (Fig. 11-B). Many of the intrusive bodies in the area are hydrothermally altered. This causes a smoother topographic surface (Figs. 12-C and D). High Radar return is observed from the unaltered intrusives and also the dacitic rocks (Figs. 11-A, B, E and 12- A, E, F). The surfaces of these rocks are texturally coarse that cause the high Radar return. An intrusive body exists in the northwest of Sar Cheshmeh mine that has a subtle indication in the processed satellite images (VNIR+SWIR) but it is shown well in the integrated images (Figs. 10-A and 12-G and H). This intrusive body has not been reported in the previous geological maps and is highly altered, but the vegetation cover on top of this body doesn't allow it to be detected by satellite images in the optical region. This also can be detected by using airborne geophysical data as reported by Ranjbar and Honarmand (2004).

The sedimentary rocks in the area are mainly the conglomerate (Fig. 11-C), calcareous terraces (Fig. 12- F), calc tufa (Travertine) (Figs. 11-D and F), alluvial fans and Recent alluvial deposits. The conglomerates are composed of pebbles from the volcanic, intrusive or altered rocks. This will have a serious effect on lithological discrimination as they may show the same spectral signature as their source
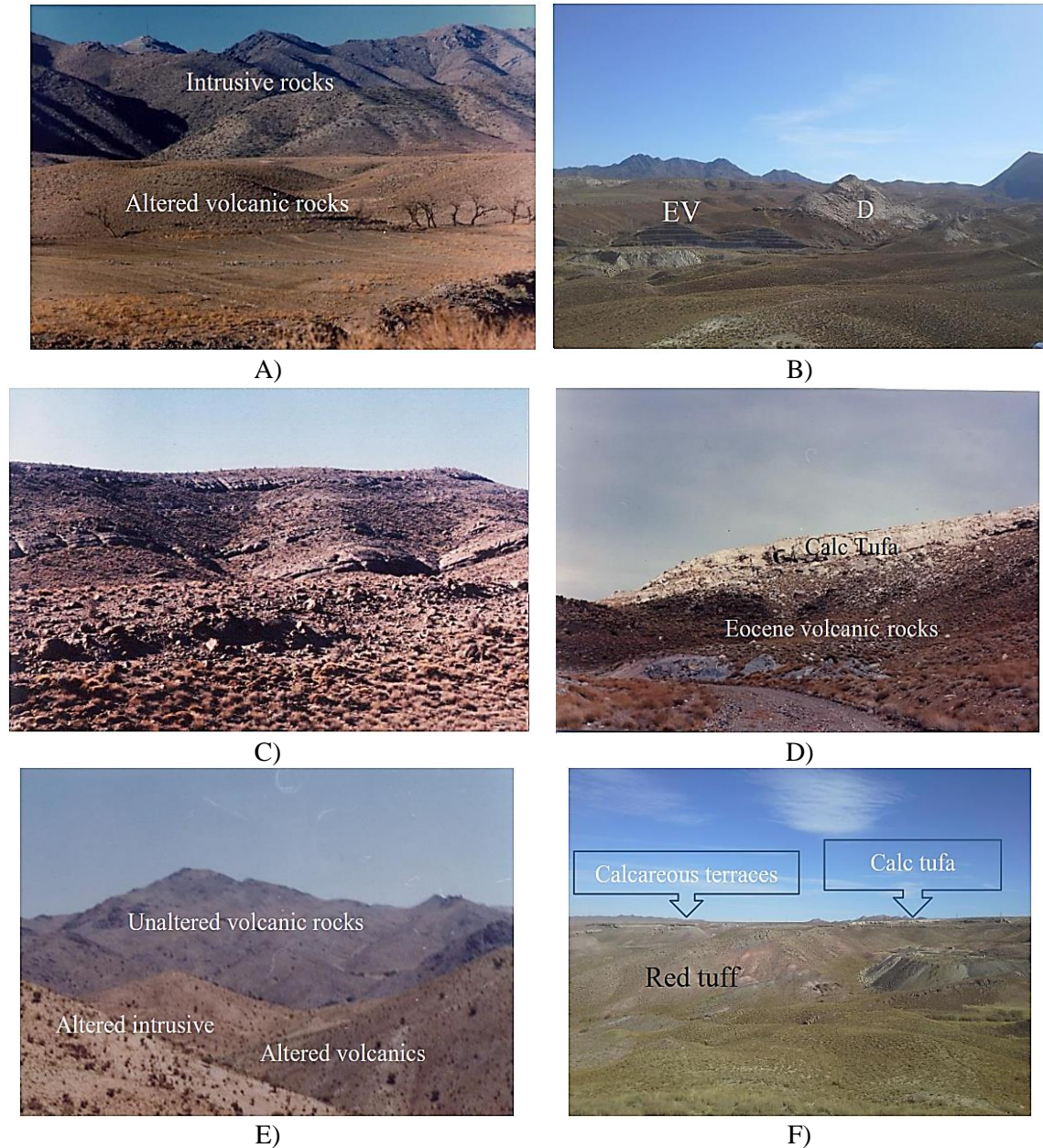
Fig. 11   A-General view of the altered volcanic rocks and the intrusive rocks (looking northwest), B- Quaternary dacite (D) which overlies the Eocene volcanic rocks (EV) (Looking south), C- Thick Layers of Neogene conglomerate in the southern part of the area (Looking north), D-Quaternary calc tuffa overlies the Eocene volcanic rocks, E- A general view of the altered volcanic and plutonic rocks in Darrrehzar area, in vicinity of the unaltered volcanic rocks, F- calcareous terraces and calc tuffa that overlie the Eocene red tuffs.

rocks; but they differ from their source rocks in terms of surface texture. Low Radar return is observed on the calc tufas, because of their smooth surface and the bedding is almost horizontal (Fig. 11-D). Although the calcareous terraces have a horizontal bedding, but they show higher Radar return than the calc tufas due to their rough surfaces (Fig. 11-F). The sedimentary rocks show different responses in the Radar images. In places where the rocks are inclined and show a rough surface, high Radar return is observed (Fig. 11-C), but in cases that the alluvial sediments have smooth texture, the Radar return is low. The alluvial fans show low Radar return due to their smoother surface as compared to the sedimentary rocks in the south of the area (Figs. 5-A and B). These subtle differences are demonstrated by the lithologies in the Radar images combined with the multispectral data, which can help in differentiating the lithologies within this area.

Results show that the lithologic units 2Ng, Mda, Ev and Altered Gd represent better overall classification in all methods and datasets. In contrast, the Razak volcanics, dacites (dc), dacitoid pyroclastics (dp) and alluvial units have the weakest overall enhancement response in classification. The Gd,
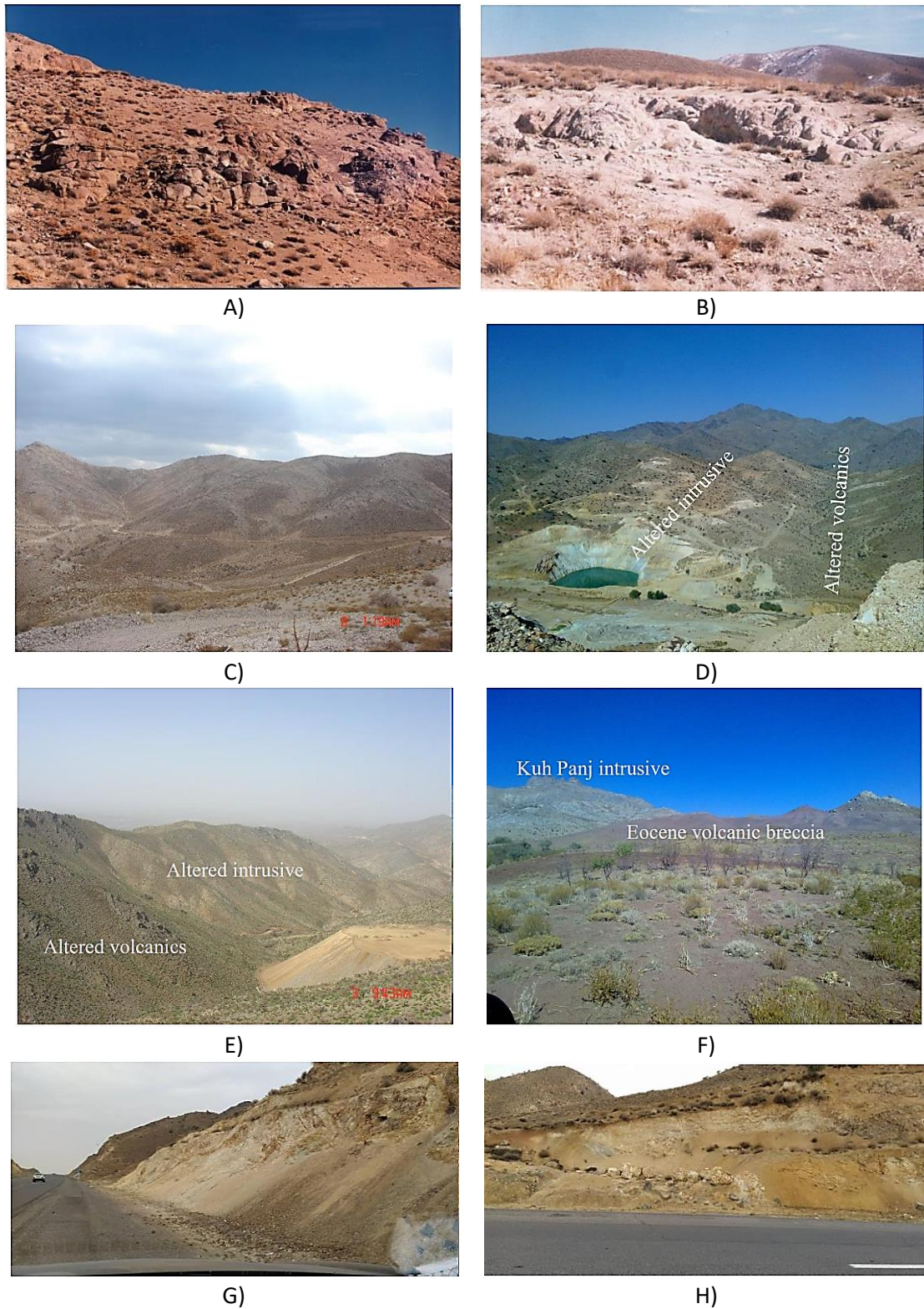
Fig. 12 The intrusive bodies in the study area. A- Dehsiahan altered monzonite, B- Baghkhoshk altered quartz monzonite, C- SarCheshmeh altered granodiorite (Looking northeast), D- Darrehzar altered granodiorite (Looking east), E- Now Chun altered granodiorite in contact with the altered volcanic rocks, F- Kuh Panj intrusive body (Looking north). G and H-The intrusive body in the northwest of SarCheshmeh mine. This is highly altered.

altered Gd and Mda units showed better enhancement using the integrated dataset in all methods but the Edv and travertine (calc tufa) units were poorly enhanced by using the integrated dataset (except in Bayesian Regularization for travertine and in Scaled Conjugate Gradient for Edv). The 2Ng units represent better enhancement using the integrated dataset except in the pattern recognition neural net fitting method (with all of its algorithms), which was also not a good choice for enhancement of alluvial sediments, dc, dp, Ev, and Water pixels. In addition, the neural net fitting method was not successful in classification of vegetated areas (except Scaled Conjugate Gradient method by using only the spectral dataset). Only the pattern recognition method recognized water pixels while all of other methods have poorly recognized water pixels. Surface water is better enhanced by using optical images. The altered Gd units represent better classification by the neural net fitting compared to the pattern recognition method.

The Bayesian Regularization algorithm spent more training time with only multispectral data than with integrated Radar-multispectral data; this shows the advantage of using the integrated data to improve the training process. It is good and considerable that integrating Radar and spectral data reduces the training time for this algorithm. In other words, by adding Radar dataset, the algorithm finds a faster and better way to learn the patterns. In the application of neural pattern recognition method to integrated data, there was less error (with fewer epochs) compared with its application to only spectral data; thus, the combination of Radar and multispectral data gave better results. With the neural net fitting method (based on Levenberg-Marquardt training algorithm), less training time was spent on integrated data than on only multispectral data although with almost similar training percentage error; this case similarly occurs with the use of the Bayesian regularization training algorithm.

5. CONCLUSIONS

- Training an ANN with combined Radar and multispectral data proved more efficient than using just multispectral data in most cases. This resulted in:
  - Less training time (especially with Bayesian regularization and Levenberg-Marquardt algorithms).
  - Lower error rates (except for the Neural Pattern Recognition method).
- Overall classification accuracy was generally higher with combined data, except for the Neural Pattern Recognition method which showed similar performance with both integrated Radar-multispectral data and only multispectral data (overall accuracy 80.09 % vs. 79.36 %).
- The Neural Pattern Recognition method achieved the best results in terms of training time, but required more training iterations.

- Other training algorithms like Bayesian Regularization, Levenberg-Marquardt, and Scaled Conjugate Gradient showed better performance compared to the Neural Net Fitting method under similar conditions.
- This study confirms the effectiveness of ANNs for geological mapping, particularly when using combined data sources like radar and multispectral imagery.
- Integrating radar data with other remote sensing sources offers a promising approach for improved results in geological mapping.

REFERENCES

Abrams, M. and Hook, S.: 2002, ASTER User Handbook, Version 2. Jet Propulsion Laboratory, 135.

Abrams, M. and Yamaguchi, Y.: 2019, Twenty years of ASTER contributions to lithologic mapping and mineral exploration. Remote Sens., 11, 1394. DOI: 10.3390/rs11111394

Alimohammadi, M., Alirezaei, S. and Kontak, D.J.: 2015, Application of ASTER data for exploration of porphyry copper deposits: A case study of Daraloo-Sarmeshk area, southern part of the Kerman copper belt, Iran. Ore Geol. Rev., 70, 290–304. DOI: 10.1016/j.oregeorev.2015.04.010

Alirezaei, S. and Hassanpour, S.: 2011, An overview of porphyry copper deposits in Iran. In: The 1st World Copper Congress, Iran, 49–62.

Almeida-Filho, R., Shimabukuro, Y.E., Rosenqvist, A. and Sánchez, G.A.: 2009, Using dual-polarized ALOS PALSAR data for detecting new fronts of deforestation in the Brazilian Amazônia. Int. J. Remote Sens., 30, 3735–3743. DOI: 10.1080/01431160902777175

Amer, R., El Mezayen, A. and Hasanein, M.: 2016, ASTER spectral analysis for alteration minerals associated with gold mineralization. Ore Geol. Rev., 75, 239–251. DOI: 10.1016/j.oregeorev.2015.12.008

Anderson, G.P., Felde, G.W., Hoke, M.L., Ratkowski, A.J., Cooley, T.W., Chetwynd, Jr., J.H., Gardner, J.A., Adler-Golden, S.M., Matthew, M.W., Berk, A., Bernstein, L.S., Acharya, P.K., Miller, D.P. and Lewis, P.E.: 2002, MODTRAN4-based atmospheric correction algorithm: FLAASH (Fast Line-of-sight Atmospheric Analysis of Spectral Hypercubes). In: Algorithms and Technologies for Multispectral, Hyperspectral, and Ultraspectral Imagery VIII. International Society for Optics and Photonics, 65–71. DOI: 10.1117/12.478737

Atapour, H.: 2007, Geochemistry and metallogenic of igneous rocks in Dehaj–Sardoieh Belt, Kerman. Doctoral dissertation, Ph. D. thesis, Shahid Bahonar University of Kerman, Iran.

Awoyera, P.O., Akinmusuru, J.O., Krishna, A.S., Gobinath, R., Arunkumar, B. and Sangeetha, G.: 2020, Model development for strength properties of laterized concrete using artificial neural network principles. In: Soft Computing for Problem Solving, 97-207 Springer, Singapore.

Azhar Omar, M., Khair Hassan, M., Che Soh, A. and Ab. Kadir, M.Z.A.: 2013, Lightning severity classification utilizing the meteorological parameters: A neural network approach. In: Proceedings - 2013 IEEE

International Conference on Control System, Computing and Engineering, ICCSCE 2013. IEEE, 111–116. DOI: 10.1109/ICCSCE.2013.6719942

Bansal, D. and Chhikara, R.: 2014, Performance evaluation of steganography tools using SVM and NPR tool: In: International Conference on Advanced Computing and Communication Technologies, ACCT. IEEE, 483–487. DOI: 10.1109/ACCT.2014.17

Bashir, M.K. and Gilani, S.A.M.: 2011, Log domain speckle noise reduction in ultrasonographic animal images. In: Advances in Intelligent and Soft Computing, Springer, 709–715. DOI: 10.1007/978-3-642-25658-5_84

Bebis, G. and Georgiopoulos, M.: 1994, Feed-forward neural networks. IEEE Potentials, 13, 4, 27–31. DOI: 10.1109/45.329294

Berberoglu, S., Lloyd, C.D., Atkinson, P.M. and Curran, P.J.: 2000, The integration of spectral and textural information using neural networks for land cover mapping in the Mediterranean. Comput. Geosci., 26, 4, 385–396.

Bharatkar, P.S. and Patel, R.: 2013, Approach to accuracy assessment tor RS image classification techniques. Int. J. Sci. Eng. Res., 4, 12, 79-86.

Bruzzone, L., Prieto, D.F. and Serpico, S.B.: 1999, A neural-statistical approach to multitemporal and multisource remote-sensing image classification. IEEE Trans. Geosci. Remote Sens., 37, 3 I, 1350–1359. DOI: 10.1109/36.763299

Cheng, G., Ding, H., Yang, J. and Cheng, Y.: 2023, Crop type classification with combined spectral, texture, and radar features of time-series Sentinel-1 and Sentinel-2 data. Int. J. Remote Sens., 44, 4, 1215-1237. DOI: 10.1080/01431161.2023.2176723

Cloutis, E.A., Connery, D.R. and Dover, F.J.: 1999, Agricultural crop monitoring using airborne multi-spectral imagery and c-band synthetic aperture radar. Int. J. Remote Sens., 20, 767–787. DOI: 10.1080/014311699213181

Cooley, T., Anderson, G.P., Felde, G.W., Hoke, M.L., Ratkowski, A.J., Chetwynd, J.H., Gardner, J.A., Adler-Golden, S.M., Matthew, M.W. and Berk, A.: 2002, FLAASH, a MODTRAN4-based atmospheric correction algorithm, its application and validation. In: IEEE International Geoscience and Remote Sensing Symposium. IEEE, 1414–1418.

Çolak, E. and Sunar, F.: 2023, Investigating the usefulness of satellite-retrieved land surface temperature (LST) in pre-and post-fire spatial analysis. Earth Sci. Inform., 16, 1, 945-963. DOI: 10.1007/s12145-022-00883-8

David, R.M., Rosser, N.J. and Donoghue, D.N.: 2022, Improving above ground biomass estimates of Southern Africa dryland forests by combining Sentinel-1 SAR and Sentinel-2 multispectral imagery. Remote Sens. Environ., 282, 113232. DOI: 10.1016/j.rse.2022.113232

del Valle, H.F., Metternicht, G.I., Tentor, F., Sione, W.F., Zamboni, P., Mayer, F.V. and Aceñolaza, P.G.: 2023, Synergistic use of radar and optical image data for improved land use and land cover assessment: A case study in the North of Entre Rios Province (Argentina). In: Geopedology, An Integration of Geomorphology and Pedology for Soil and Landscape Studies, 283-314. Cham: Springer International Publishing. DOI: 10.1007/978-3-031-20667-2_15

Delalleau, O. and Bengio, Y.: 2011, Shallow vs. deep sum-product networks. In: Advances in Neural Information Processing Systems, 666–674.

Dimitrijevic, M.N.: 1971, Geological map of Chahargonbad, sheet no. 7249, 1: 100,000 series. Geological Survey of Iran, Tehran.

Dimitrijevic, M.D., Dimitrijevic, M.N., Djordjevic, M. and Vulovic, D.: 1971a, Geological map of Pariz, sheet no. 7149, 1: 100,000 series. Geological Survey of Iran.

Dimitrijevic, M.D., Dimitrijevic, M.N., Djordjevic, M. and Djokovic, I.: 1971b, Geological map of Rafsanjan II, sheet 7250, Geological Survey of Iran, Tehran.

Dimitrijevic, M.D.: 1973a, Geology of Kerman region. Geological Survey of Iran, Tehran 334.

Dimitrijevic, M.D., Dimitrijevic, M.N. and Djordjevic, M.: 1973b, Geological map of Rafsanjan 1, No. 7150, Series 1: 100,000. Geological Survey of Iran, Tehran.

Edoho, M., Ekpenyong, M. and Inyang, U.: 2018, Speech features analysis for tone language speaker discrimination systems. In: Latifi, S. (eds), Information Technology - New Generations. Advances in Intelligent Systems and Computing, 738. Springer, Cham. DOI: 10.1007/978-3-319-77028-4_57

Gabr, S.S., Hassan, S.M. and Sadek, M.F.: 2015, Prospecting for new gold-bearing alteration zones at El-Hoteib area, South Eastern Desert, Egypt, using remote sensing data analysis. Ore Geol. Rev., 71, 1–13. DOI: 10.1016/j.oregeorev.2015.04.021

García, M., Saatchi, S., Ustin, S. and Balzter, H.: 2018, Modelling forest canopy height by integrating airborne LiDAR samples with satellite Radar and multispectral imagery. Int. J. Appl. Earth Obs. Geoinf., 66, 159–173. DOI: 10.1016/j.jag.2017.11.017

Ghorashi-Zadeh, M.: 1978, Development of hypogene and supergene alteration and copper mineralization patterns, Sar Cheshmeh porphyry copper deposits, Iran. Brock University.

Goward, S.N., Masek, J.G., Williams, D.L., Irons, J.R. and Thompson, R.J.: 2001, The Landsat 7 mission: Terrestrial research and applications for the 21st century. Remote Sens. Environ., 78, 3–12. DOI: 10.1016/S0034-4257(01)00262-0

Grebby, S., Naden, J., Cunningham, D. and Tansey, K.: 2011, Integrating airborne multispectral imagery and airborne LiDAR data for enhanced lithological mapping in vegetated terrain. Remote Sens. Environ., 115, 214–226. DOI: 10.1016/j.rse.2010.08.019

Guha, A. and Vinod Kumar, K.: 2016, New ASTER derived thermal indices to delineate mineralogy of different granitoids of an Archaean Craton and analysis of their potentials with reference to Ninomiya's indices for delineating quartz and mafic minerals of granitoids-An analysis in Dharwar Craton, India. Ore Geol. Rev., 74, 76–87. DOI: 10.1016/j.oregeorev.2015.10.033

Hajaj, S., El Harti, A. and Jellouli, A.: 2022, Assessment of hyperspectral, multispectral, radar, and digital elevation model data in structural lineaments mapping: A case study from Ameln valley shear zone, Western Anti-Atlas Morocco. Remote Sens. Appl. Soc. Environ., 27, 100819. DOI: 10.1016/j.rsase.2022.100819

Hassanzadeh, J.: 1994, Metallogenic and tectonomagmatic events in the SE sector of the Cenozoic active continental margin of central Iran (Shahr-e-Babak area, Kerman Province). Doctoral dissertation, Ph.D. thesis, University of California, Los Angeles.

Ibáñez Civera, J., Garcia Breijo, E., Laguarda Miró, N., Gil Sánchez, L., Garrigues Baixauli, J., Romero Gil, I., Masot Peris, R. and Alcañiz Fillol, M.: 2011, Artificial

neural network onto eight-bit microcontroller for Secchi depth calculation. Sens. Actuators, B Chem., 156, 132–139. DOI: 10.1016/j.snb.2011.04.001

Joshi, N., Baumann, M., Ehammer, A., Fensholt, R., Grogan, K., Hostert, P., Jepsen, M.R., Kuemmerle, T., Meyfroidt, P., Mitchard, E.T.A., Reiche, J., Ryan, C.M. and Waske, B.: 2016, A review of the application of optical and radar remote sensing data fusion to land use mapping and monitoring. Remote Sens., 8, 70. DOI: 10.3390/rs8010070

Kamal El-Din, G.M., El-Noby, E., Abdelkareem, M. and Hamimi, Z.: 2021, Using multispectral and radar remote sensing data for geological investigation, Qena-Safaga Shear Zone, Eastern Desert, Egypt. Arab. J. Geosci., 14, 11, 997.
DOI: 10.1007/s12517-021-07130-2

Kohli, M.D., Summers, R.M. and Geis, J.R.: 2017, Medical image data and datasets in the Era of Machine Learning—Whitepaper from the 2016 C-MIMI Meeting Dataset Session. J. Digit. Imaging, 30, 392–399. DOI: 10.1007/s10278-017-9976-3

Kose, U. and Arslan, A.: 2017, Optimization of self-learning in computer engineering courses: An intelligent software system supported by Artificial Neural Network and Vortex Optimization Algorithm. Comput. Appl. Eng. Educ., 25, 142–156.
DOI: 10.1002/cae.21787

Kulkarni, S.C., Rege, P.P. and Parishwad, O.: 2019, Hybrid fusion approach for synthetic aperture radar and multispectral imagery for improvement in land use land cover classification. J. Appl. Remote Sens., 13, 1.
DOI: 10.1117/1.jrs.13.034516

Kumar, S., Pandey, M.K., Nath, A. and Subbiah, K.: 2016, Missing QoS-values predictions using neural networks for cloud computing environments. In: 2015 International Conference on Computing and Network Communications, CoCoNet 2015. IEEE, 414–419. DOI: 10.1109/CoCoNet.2015.7411219

Li, A., Yan, X. and Kang, X.: 2023, Applicability study of four atmospheric correction methods in the remote sensing of lake water color. Geocarto Int., 38, 1, 224-282. DOI: 10.1080/10106049.2023.2240282

Li, M., Zeng, Y., Lubczynski, M.W., Roy, J., Yu, L., Qian, H., ... and Su, Z.: 2021, A first investigation of hydrogeology and hydrogeophysics of the Maqu catchment in the Yellow River source region. Earth Syst. Sci. Data Discuss., 13, 4727-4757.
DOI: 10.5194/essd-2020-230

Liu, R., Asemota, G.N.O., Benimana, S., Nduwamungu, A., Bimenyimana, S. and Niyonteze, J.D.D.: 2020, Comparison of nonlinear autoregressive neural networks without and with external inputs for PV Output Power Prediction. In: 2020 IEEE International Conference on Artificial Intelligence and Information Systems (ICAIIS), 145-149.
DOI: 10.1109/ICAIIS49377.2020.9194878

Logan, T.A., Nicoll, J., Laurencelle, J., Hogenson, K., Gens, R., Buechler, B., Barton, B., Shreve, W., Stern, T., Drew, L. and Guritz, R.: 2014, Radiometrically terrain corrected ALOS PALSAR data available from the Alaska Satellite Facility. Am. Geophys. Union 2014, IN33B-3762.

McInnes, B.I.A., Evans, N.J., Belousova, E., Griffin, W.T. and Andrew, R.L.: 2003, Timing of mineralization and exhumation processes at the Sar Cheshmeh and Meiduk porphyry Cu deposits, Kerman belt, Iran. In: Eliopoulos et al. (ed.), Mineral Exploration and Sustainable Development. Rotterdam, Millpress, 41, 1197–1200.

Mehta, P., Das, P., Bajpai, A. and Bist, A.S.: 2016, Image classification using NPR and comparison of classification results. In: Proceedings of the 10th INDIACom; 2016 3rd International Conference on Computing for Sustainable Global Development, INDIACom 2016. IEEE, 3231–3234.

Miao, J., Zhou, X., Huang, T.Z., Zhang, T. and Zhou, Z.: 2019, A novel inpainting algorithm for recovering Landsat-7 ETM+ SLC-OFF images based on the low-rank approximate regularization method of dictionary learning with nonlocal and nonconvex models. IEEE Trans. Geosci. Remote Sens., 57, 6741–6754.
DOI: 10.1109/TGRS.2019.2908381

Montanaro, A., Valsesia, D., Fracastoro, G. and Magli, E.: 2022, Semi-supervised learning for joint SAR and multispectral land cover classification. IEEE Geosci. Remote Sens. Lett., 19, 1–5.
DOI: 10.1109/LGRS.2022.3195259

Mouret, F.: 2022, Crop monitoring and detection of anomalous crop development at the parcel-level with multispectral and synthetic aperture radar satellite data. Doctoral dissertation, Ph.D. thesis.
DOI: 10.13140/RG.2.2.32828.72329

Movchan, D., Bilous, A., Yelistratova, L., Apostolov, A. and Hodorovsky, A.: 2023, Application of various approaches of multispectral and radar data fusion for modelling of aboveground forest biomass. Folia For. Pol., 65, 2, 55-67. DOI: 10.2478/ffp-2023-0006

Nasab, M.H. and Agah, A.: 2023, Mapping hydrothermal alteration zones associated with copper mineralization using ASTER data: a case study from the Mirjaveh area, southeast Iran. Trans. A Basics, 36, 4, 720-732.
DOI: 10.5829/IJE.2023.36.04A.11

Neapolitan, R.E.: 2018, Neural networks and deep learning, artificial intelligence. Determination press, San Francisco, CA. DOI: 10.1201/b22400-15

Nielsen, M.: 2018, Neural networks and deep learning.
DOI: 10.1201/b22400-15

Pal, S.K., Majumdar, T.J. and Bhattacharya, A.K.: 2007, ERS-2 SAR and IRS-1C LISS III data fusion: a PCA approach to improve remote sensing based geological interpretation. ISPRS J. Photogramm. Remote Sens., 61, 281–297. DOI: 10.1016/j.isprsjprs.2006.10.001

Palaniyandi, M., Manivel, P., Sharmila, T. and Thirumalai, P.: 2021, The use of Multispectral (MSS) and Synthetic Aperture Radar (SAR) microwave remote sensing data to study environment variables, land use/land cover changes, and recurrent weather condition for forecast malaria: A systematic review. Appl. Ecol. Environ. Sci., 9, 4, 490-501.
DOI: 10.12691/aees-9-4-10

Papale, L.G., Guerrisi, G., De Santis, D., Schiavon, G. and Del Frate, F.: 2023, Satellite data potentialities in solid waste landfill monitoring: Review and case studies. Sensors, 23, 8, 3917. DOI: 10.3390/s23083917

Pour, A.B. and Hashim, M.: 2014, Structural geology mapping using PALSAR data in the Bau gold mining district, Sarawak, Malaysia. Adv. Sp. Res., 54, 644–654. DOI: 10.1016/j.asr.2014.02.012

Pour, A.B., Hashim, M. and van Genderen, J.: 2013, Detection of hydrothermal alteration zones in a tropical region using satellite remote sensing data: Bau goldfield, Sarawak, Malaysia. Ore Geol. Rev., 54, 181–196. DOI: 10.1016/j.oregeorev.2013.03.010

Pournamdari, M., Hashim, M. and Pour, A.B.: 2014a, Application of ASTER and Landsat TM data for geological mapping of Esfandagheh ophiolite complex, southern Iran. Resour. Geol., 64, 233–246. DOI: 10.1111/rge.12038

Pournamdari, M., Hashim, M., Pour, A.B.: 2014b, Spectral transformation of ASTER and Landsat TM bands for lithological mapping of Soghan ophiolite complex, south Iran. Adv. Sp. Res., 54, 694–709. DOI: 10.1016/j.asr.2014.04.022

Prisciandaro, E., Sedda, G., Cara, A., Diotti, C., Spaggiari, L. and Bertolaccini, L.: 2023, Artificial neural networks in lung cancer research: A narrative review. J. Clin. Med., 12, 3, 880. DOI: 10.3390/jcm12030880

Rahmani, N., Ranjbar, H. and Nezamabadi-pour, H.: 2020, Multi-Spectral and RADAR data fusion for improving geological mapping accuracy. Kharazmi J. Earth Sci. 6, 1, 151-168. DOI: 10.52547/gnf.6.1.151

Rani, K., Guha, A., Mondal, S., Pal, S.K. and Vinod Kumar, K.: 2019, ASTER multispectral bands, ground magnetic data, ground spectroscopy and space-based EIGEN6C4 gravity data model for identifying potential zones for gold sulphide mineralization in Bhukia, Rajasthan, India. J. Appl. Geophys., 160, 28–46. DOI: 10.1016/j.jappgeo.2018.10.001

Ranjbar, H. and Honarmand, M.: 2004, Integration and analysis of airborne geophysical and ETM+ data for exploration of porphyry type deposits in the Central Iranian Volcanic Belt using fuzzy classification. Int. J. Remote Sens., 25, 21, 4729-4741. DOI: 10.1080/01431160410001709011

Research Systems, Inc.: 2003, Environment for visualizing images (ENVI) user's guide. Boulder, 1084 pp.

Righini, M., Valentini, E., Sapio, S., Marinelli, C., Gatti, I., Jimenez, M. J., ... and Taramelli, A.: 2022, Synergic application of synthetic aperture radar, multispectral and hyperspectral data, using a multi-temporal approach for land cover mapping. In: AGU Fall Meeting Abstracts, 2022, B32A-04.

Rosenqvist, A., Shimada, M., Ito, N. and Watanabe, M.: 2007, ALOS PALSAR: A pathfinder mission for global-scale monitoring of the environment. IEEE Trans. Geosci. Remote Sens., 45, 3307–3316. DOI: 10.1109/TGRS.2007.901027

Rosenqvist, A., Shimada, M., Suzuki, S., Ohgushi, F., Tadono, T., Watanabe, M., Tsuzuku, K., Watanabe, T., Kamijo, S., Aoki, E., 2014. Operational performance of the ALOS global systematic acquisition strategy and observation plans for ALOS-2 PALSAR-2. Remote Sens. Environ., 155, 3–12. DOI: 10.1016/j.rse.2014.04.011

Sabzehei, M., Ghandchi, M., Jaliliyan, M. and Afaghi, A.: 1994, Geological map of Kerman Province (With 1:500000 scale). Plan and budget organization of Iran, Kerman.

Safari, M., Maghsoudi, A. and Pour, A.B.: 2018, Application of Landsat-8 and ASTER satellite remote sensing data for porphyry copper exploration: a case study from Shahr-e-Babak, Kerman, south of Iran. Geocarto Int., 33, 1186–1201. DOI: 10.1080/10106049.2017.1334834

Salem, S.M., El Sharkawi, M., El-Alfy, Z., Soliman, N.M. and Ahmed, S.E.: 2016, Exploration of gold occurrences in alteration zones at Dungash district, Southeastern Desert of Egypt using ASTER data and geochemical analyses. J. Afr. Earth Sci., 117, 389–400. DOI: 10.1016/j.jafrearsci.2016.01.030

Shafiei, B., Haschke, M. and Shahabpour, J.: 2009, Recycling of orogenic arc crust triggers porphyry Cu mineralization in Kerman Cenozoic arc rocks, southeastern Iran. Miner. Depos., 44, 265–283. DOI: 10.1007/s00126-008-0216-0

Tetko, I.V., Livingstone, D.J. and Luik, A.I.: 1995, Neural network studies. 1. Comparison of overfitting and overtraining. J. Chem. Inf. Comput. Sci., 35, 826–833. DOI: 10.1021/ci00027a006

Thurmond, A.K., Abdelsalam, M.G. and Thurmond, J.B.: 2006, Optical-radar-DEM remote sensing data integration for geological mapping in the Afar Depression, Ethiopia. J. Afr. Earth Sci., 44, 2, 119-134. DOI: 10.1016/j.jafrearsci.2005.10.006

Upreti, M. and Kumar, D.: 2021, Investigating capability of open archive multispectral and SAR datasets for Wheat crop monitoring and acreage estimation studies. Earth Sci. Inform., 14, 4, 2017-2035. DOI: 10.1007/s12145-021-00656-9

USGS, U.S. Geological Survey: 2019, Landsat Level-1 Processing Details.

Vafaei, S., Fathizadeh, O., Puletti, N., Fadaei, H., Baqer Rasooli, S. and Vaglio Laurin, G.: 2021, Estimation of forest leaf area index using satellite multispectral and synthetic aperture radar data in Iran. iForest-Biogeosciences and Forestry, 14, 3, 278. DOI: 10.3832/ifor3633-014

Yuan, L., Zhu, G. and Xu, C.: 2020, Combining synthetic aperture radar and multispectral images for land cover classification: a case study of Beijing, China. J. Appl. Remote Sens, 14, 1. DOI: 10.1117/1.jrs.14.026510

Yuhendra, Y., Alimuddin, I., Sumantyo, J.T.S. and Kuze, H.: 2012, Assessment of pan-sharpening methods applied to image fusion of remotely sensed multi-band data. Int. J. Appl. Earth Obs. Geoinf., 18, 165–175. DOI: 10.1016/j.jag.2012.01.013

Zafaty, O., Oukassou, M., Mhamdi, H.S., Tabuce, R. and Charrière, A.: 2023, Integrated remote sensing data and field investigations for geological mapping and structural analysis. The case of SW Tichoukt ridge (Middle Atlas, Morocco). J. Afr. Earth Sci., 198, 104784. DOI: 10.1016/j.jafrearsci.2022.104784

Zhang, D., Gade, M. and Zhang, J.: 2021, SOFNet: SAR-Optical fusion network for land cover classification. In: 2021 IEEE International Geoscience and Remote Sensing Symposium IGARSS, 2409-2412. DOI: 10.1109/IGARSS47720.2021.9554070

Zhang, X., Zhao, Z., Chen, Q., Chai, W., Li, Z., Zhang, G., ... and Niu, L.: 2023, Mapping hydrothermal alteration of the Pulang porphyry copper deposit, SW China, using ASTER and ZY1-02D satellite data. Ore Geol. Rev., 105605. DOI: 10.1016/j.oregeorev.2023.105605

Zoheir, B., Emam, A., Abdel-Wahed, M. and Soliman, N.: 2019, Multispectral and radar data for the setting of gold mineralization in the South Eastern Desert, Egypt. Remote Sens., 11, 1450. DOI: 10.3390/rs11121450